Supporting information

Shining light on the ferrous analogue: Excited state dynamics of an Fe(II) *hexa*-carbene scorpionate complex

Catherine E. Johnson,[a] Mawuli Deegbey,[b] Aleksandra Ilic,[c] Nidhi Kaul,[a] Om Prakash,[c] Kenneth Wärnmark,*[c] Elena Jakubikova,*[b] Reiner Lomoth*[a]

[a]Department of Chemistry–Ångström Laboratory, Uppsala University, SE-75120 Uppsala, Sweden.

[b]Department of Chemistry, North Carolina State University, 2620 Yarbrough Dr., Raleigh, North Carolina 27695, United States.

[c]Centre for Analysis and Synthesis (CAS), Department of Chemistry, Lund University, SE-22100 Lund, Sweden.

*Corresponding Authors:

E-mail: kenneth.warnmark@chem.lu.se
E-mail: ejakubi@ncsu.edu
E-mail: reiner.lomoth@kemi.uu.se

Table of Contents

In Situ Preparation of ([Fe(II)(phtmeimb)2])

Chemical reduction

All solvents and reagents as well as deuterated solvents for NMR-spectroscopy were purchased from Sigma-Aldrich and Acros Organics and used without further purification unless otherwise stated. $[Fe(phtmeimb)_2]PF_6$ was prepared according to literature protocol.[1]

Bis(phenyltris(3-methylimidazol-2-ylidene)borate)iron(III) hexafluorophosphate (40 mg, 0.046 mmol) was suspended in degassed THF-d_8 (0.3 mL) inside a glovebox. $LiAlH_4$ (2.6 mg, 0.069 mmol) in degassed THF-d_8 (0.3 mL) was added dropwise at room temperature leading to the burgundy red suspension changing color to afford a yellow solution. The reaction mixture containing $[Fe(II)(phtmeimb)_2]$ was stirred for 20 min before transferring to a J. Young NMR tube. ^{1}H NMR (400 MHz, THF-d_8) δ (ppm) = 8.19 – 8.12 (m, 4H, *H-2*), 7.51 – 7.43 (m, 4H, *H-3*), 7.38 (d, *J* = 7.3 Hz, 2H, *H-4*), 7.01 (d, *J* = 1.7 Hz, 6H, *H-5*), 6.55 (d, *J* = 1.8 Hz, 6H, *H-6*), 2.17 (s, 18H, *H-8*).^{13}C NMR (101 MHz, THF-d_8): δ (ppm) = 216.9 (*C-7*), 134.9 (*C-2*), 127.0 (*C-3*), 126.3 (*C-4*), 120.9 (*C-5*), 117.8 (*C-6*), 32.8 (*C-8*).

Note: Attempts at isolating the complex $[Fe(II)(phtmeimb)_2]$ were made, however upon removal of the reductant $LiAlH_4$, oxidation of the bright yellow powder was observed even inside the glovebox. Therefore, NMR characterization and photostability tests were performed exclusively in presence of excess $LiAlH_4$.

NMR Characterisation

NMR spectra were recorded at ambient temperature on a BrukerAvance II 400 MHz NMR spectrometer (400/101 ^{1}H/^{13}C). Chemical shifts (d) for ^{1}H and ^{13}C NMR spectra were reported in parts per million (ppm), relative to the residual solvent peak of the respective NMR solvent (THF-d_8 (δ_H = 1.72 & 3.58 and δ_C = 25.3 & 67.2 ppm)). Coupling constants (*J*) are given in Hertz (Hz), with the multiplicities being denoted as follows: singlet (s), doublet (d), triplet (t), quartet (q), quintet (qi), multiplet (m), broad (br). NMR spectra for ^{13}C were recorded with decoupling from ^{1}H.

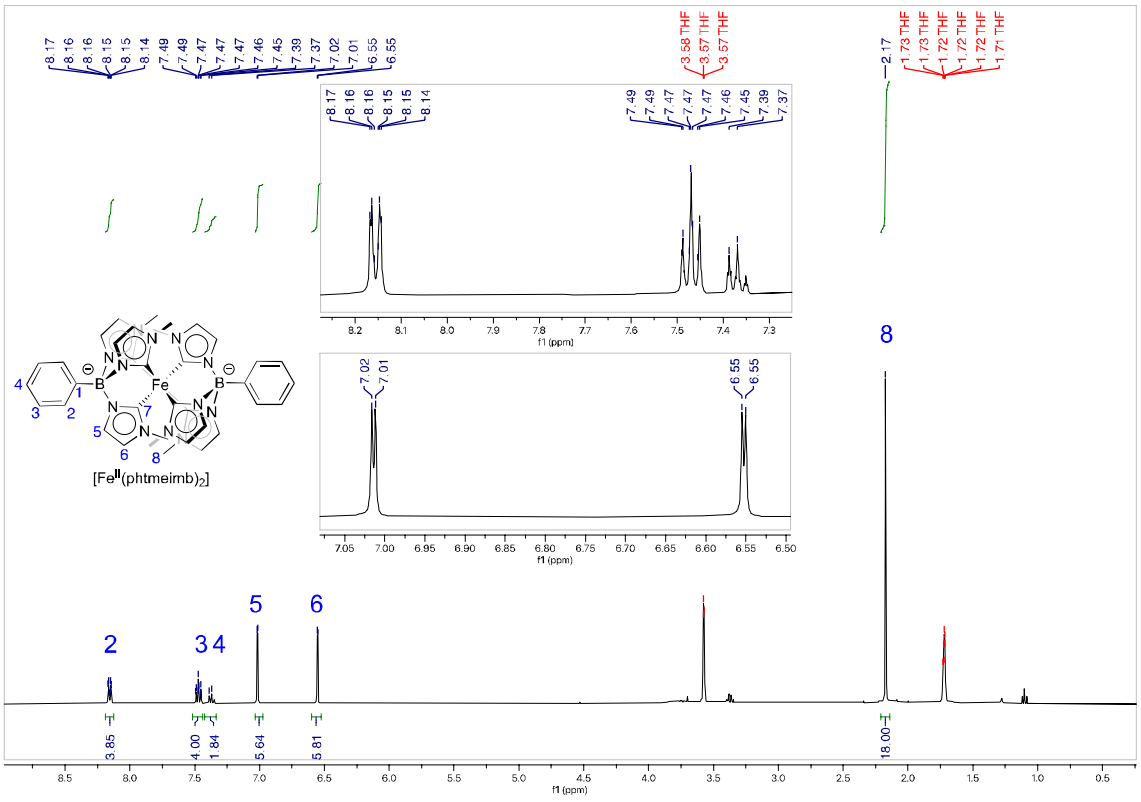

Figure S1: ^{1}H NMR spectrum (400 MHz) of [Fe(II)(phtmeimb)$_2$] with 1.5 equiv. $LiAlH_4$ in THF-d_8.

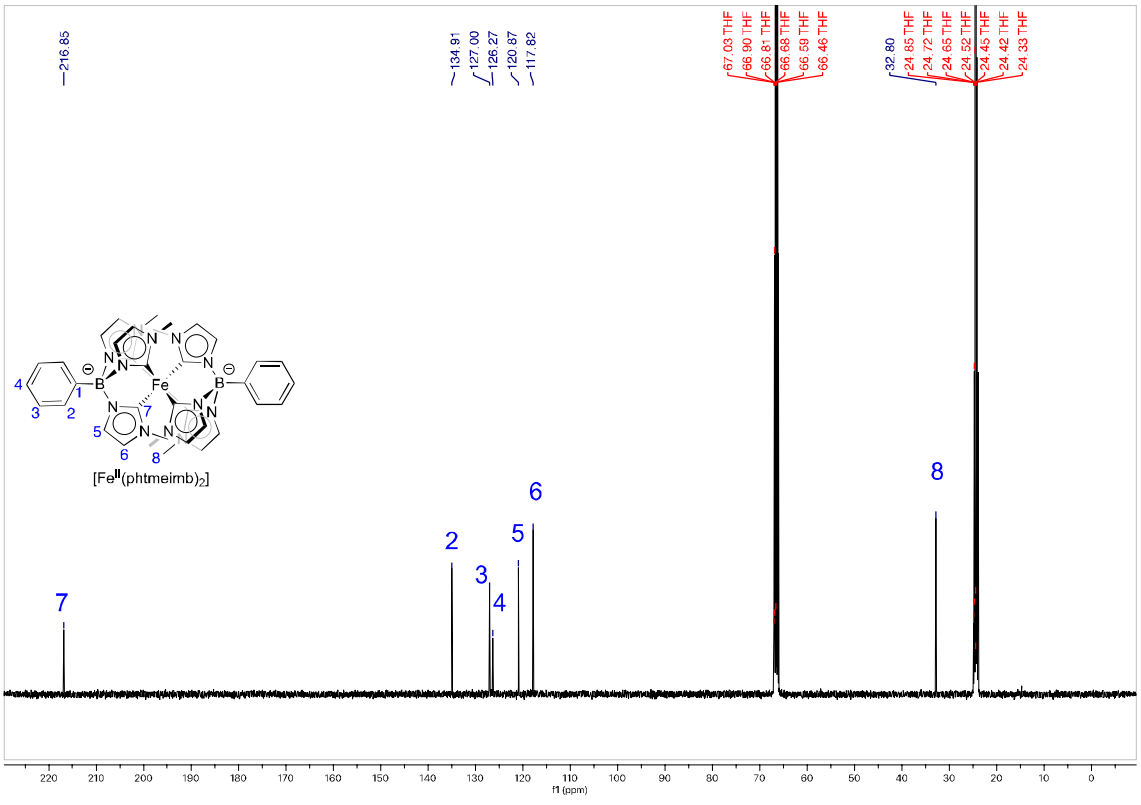

Figure S2: ^{13}C NMR spectrum (101 MHz) of [Fe(II)(phtmeimb)$_2$] with 1.5 equiv. $LiAlH_4$ in THF-d_8.

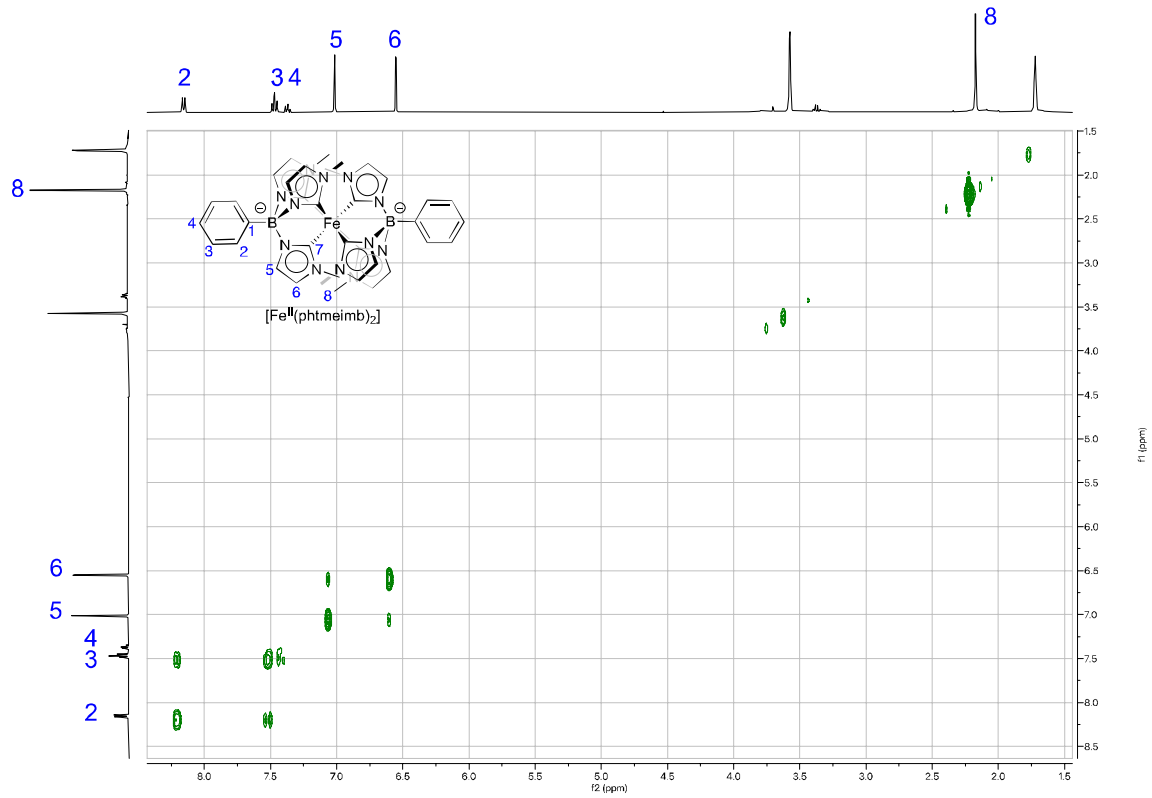

Figure S3: COSY NMR spectrum of [Fe(II)(phtmeimb)$_2$] with 1.5 equiv. $LiAlH_4$ in THF-d_8.

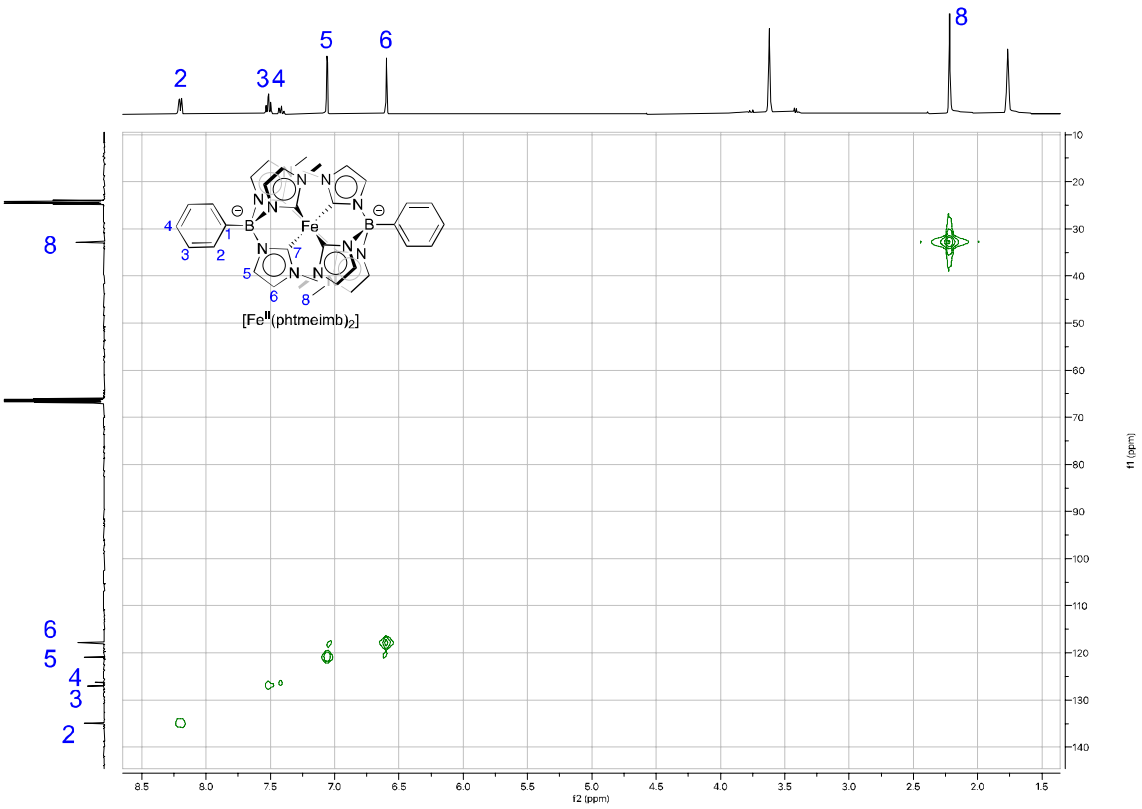

Figure S4: HMQC NMR spectrum of [Fe(II)(phtmeimb)$_2$] with 1.5 equiv. $LiAlH_4$ in THF-d_8.

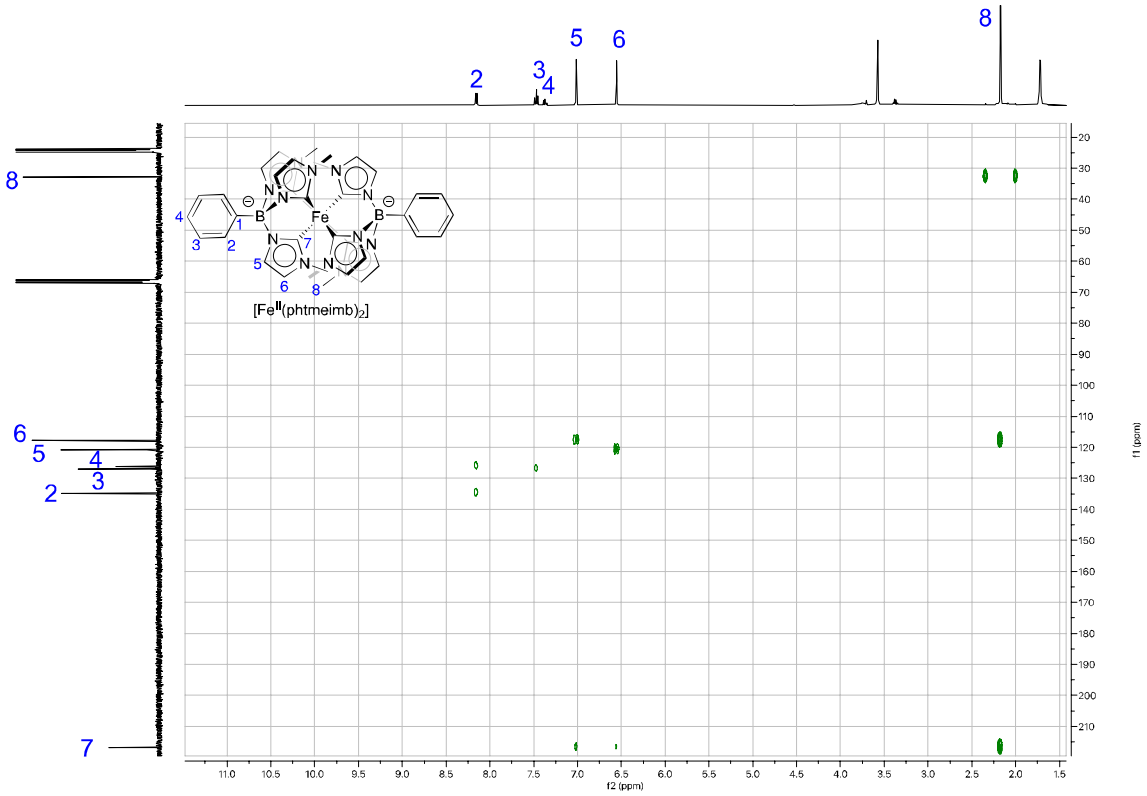

Figure S5: HMBC NMR spectrum of [Fe(II)(phtmeimb)$_2$] with 1.5 equiv. $LiAlH_4$ in THF-d_8.

Photostability

Photostability studies were performed using custom-made LED arrays (λ = 375 nm). The samples were contained in a 10 × 10 mm absorption quartz cuvette with a screw cap and PTFE septum and UV-vis absorption spectra were performed on a Probe Drum Lab-in-a-box spectrometer. Samples for photostability studies were prepared following the procedure described above. Non-deuterated degassed, anhydrous THF (distilled over Na/benzophenone) was used and the reactions were performed under argon atmosphere.

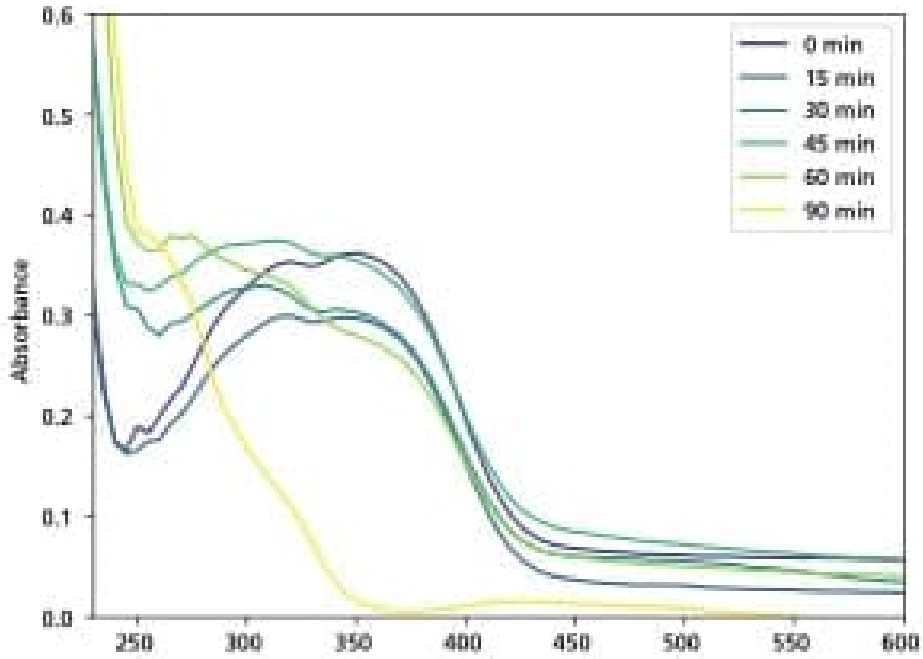

Figure S6: Photostability study for [Fe(II)(phtmeimb)$_2$] (0.3 mM) under irradiation at 375 nm (in THF + 1.5 equiv. $LiAlH_4$).

Ground State Absorption Spectra

UV-Vis absorption spectra were recorded on an Agilent 8453 or Varian Cary 50 spectrophotometer. Spectra of $[Fe(III)(phtmeimb)_2]PF_6$ and the product obtained by reduction with $LiAlH_4$ (2 M in THF, Sigma-Aldrich) revealed absorption spectra that are essentially identical to the established spectra of $[Fe(III)(phtmeimb)_2]^+$ and $[Fe(II)(phtmeimb)_2]$ in acetonitrile solution, except a very minor red shift of the LMCT (505 nm, +3 nm) and MLCT (352nm, +5 nm) bands in THF relative to acetonitrile.

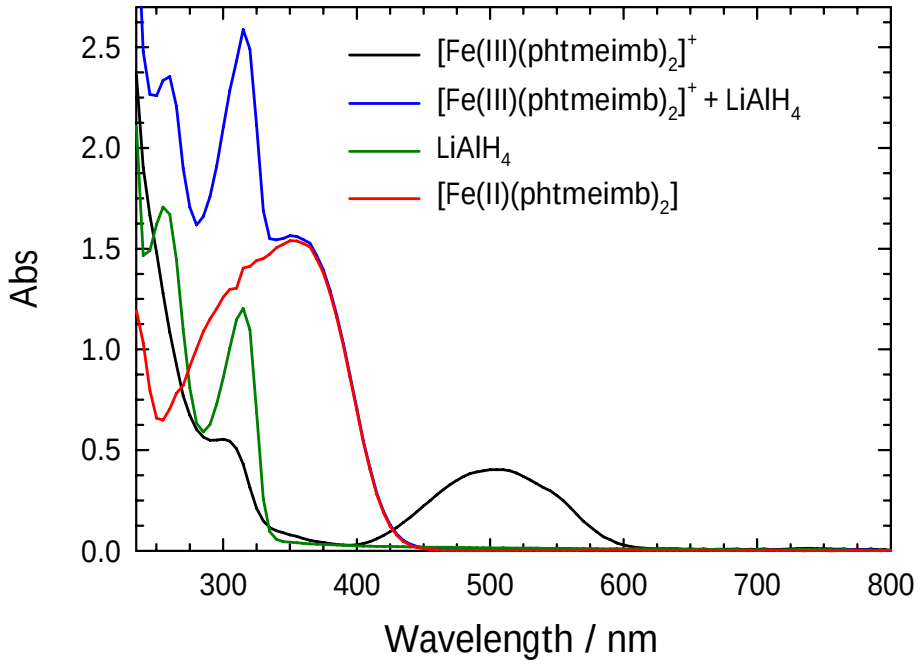

Figure S7: UV-Vis absorption spectra of $[Fe(III)(phtmeimb)_2]^+$ in THF solution (ca. 0.1 mM, l = 1 cm) before and after addition of $LiAlH_4$. Spectrum of $[Fe(II)(phtmeimb)_2]$ corrected for absorption of excess reductant.

Transient Absorption Spectra and Global and Target Analysis

Chemically-reduced sample

For transient absorption measurements, $[Fe(II)(phtmeimb)_2]$ samples were obtained by reducing $[Fe(III)(phtmeimb)_2]^+$ with $LiAlH_4$. The samples contained a slight excess of the reductant over the iron complex corresponding to a concentration on the order of 10^{-3} M. The presence of some residual reductant or products of the latter should hence not affect excited state decay kinetics on the time scale

of the transient absorption measurements. Femtosecond transient absorption measurements were carried out in a setup previously described[2, 3] using either 400 nm pump pulses from a frequency-doubled Ti:Sapphire amplifier (Coherent Libra, 3 kHz, 1.5 mJ, fwhm ~40 fs) or 350 nm, generated by the optical parametric amplifiers (TOPAS-C, Light Conversion). White light supercontinuum probe pulses were obtained by focusing the fundamental of the amplifier on a CaF_2 crystal and the probe spectrum was detected using a custom-made silicon diode array from Newport. Pump-probe overlap was optimized at the sample.

Femtosecond transient absorption measurements in THF were showing prominent cross phase modulation effects that could be also observed in control experiments with neat THF (Fig. S8).

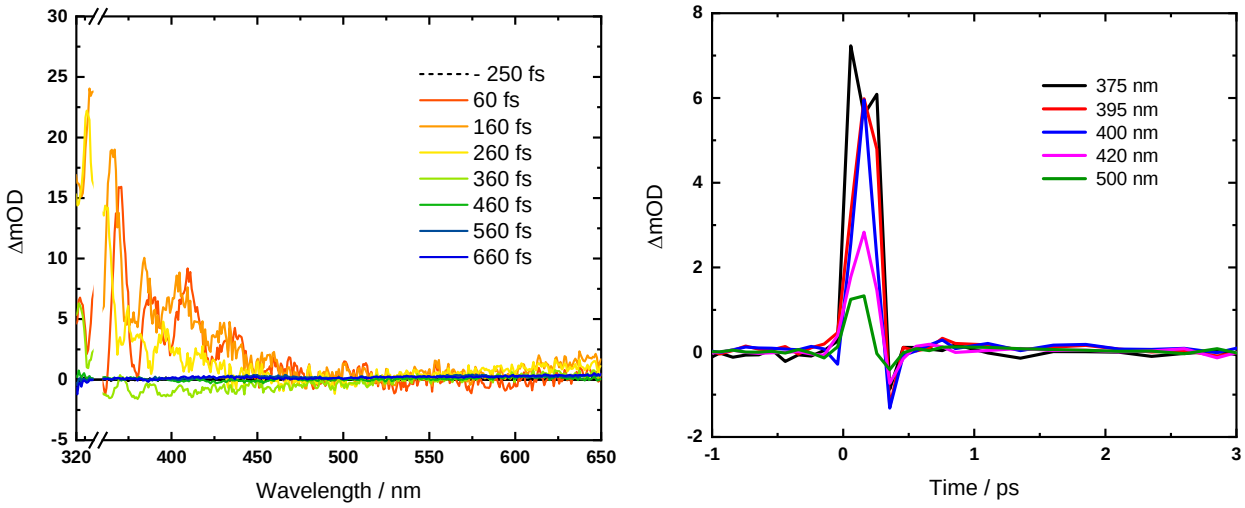

Figure S8: left: Transient absorption spectra of a blank THF sample at indicated time delays after excitation at 350 nm (~ 0.5 mW). right: Kinetic traces of a blank THF sample at indicated wavelengths after excitation at 350 nm (~ 0.5 mW).

Global and Target Analysis were performed on transient absorption spectroscopy data obtained for the chemically-reduced [Fe(II)(phtmeimb)$_2$] samples using the Glotaran 1.5.1 software.[4] The initial 400 fs were excluded from data fitting due to the strong cross-phase modulation as mentioned above.

Figure below illustrates the three different fitting models used (left: sequential; middle: parallel; right: combination of both sequential and parallel).

a)

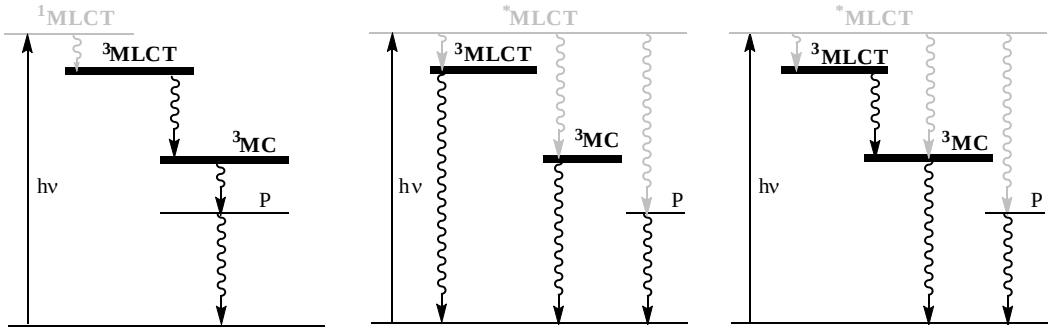
1MLCT
3MLCT
3MC
hν
P
*MLCT
3MLCT
3MC
hν
P
*MLCT
3MLCT
3MC
hν
P

b)

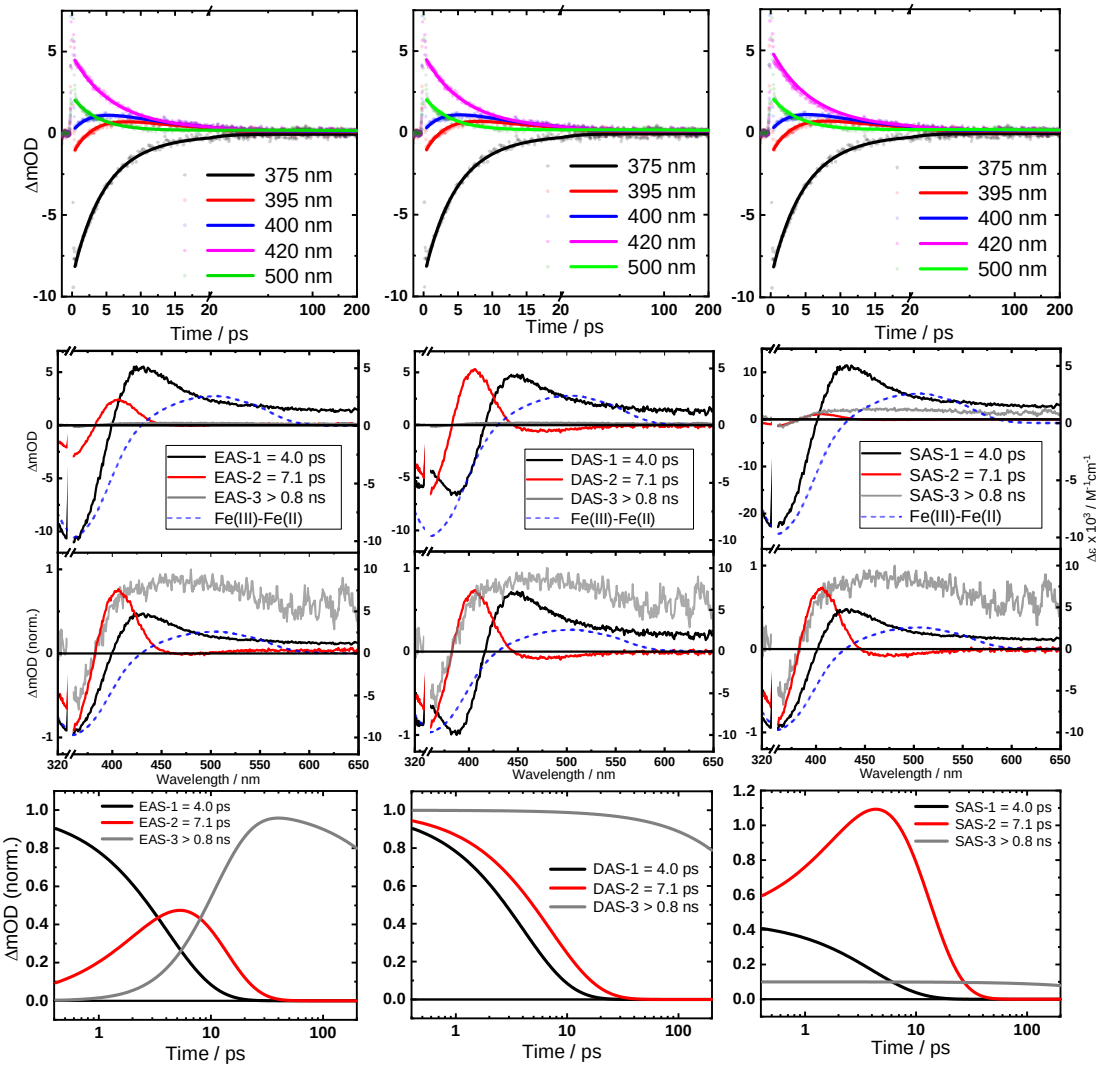
ΔmOD
Time / ps
375 nm
395 nm
400 nm
420 nm
500 nm
EAS-1 = 4.0 ps
EAS-2 = 7.1 ps
EAS-3 > 0.8 ns
Fe(III)-Fe(II)
DAS-1 = 4.0 ps
DAS-2 = 7.1 ps
DAS-3 > 0.8 ns
SAS-1 = 4.0 ps
SAS-2 = 7.1 ps
SAS-3 > 0.8 ns
ΔmOD (norm.)
Wavelength / nm
Δε x 10³ / M⁻¹cm⁻¹

Figure S9: a) Schematic state energy diagrams representing the considered fit models based on a sequential (left), parallel (middle) and combined parallel/sequential scheme (right). *MLCT represents an unresolved precursor (1MLCT or vibrationally unrelaxed 3MLCT state). P represents an unidentified product. b) Fit results for TA data after excitation of [Fe(II)(phtmeimb)$_2$] in THF at 350 nm obtained by Global Analysis/Target Analysis (fits excluding data before 400 fs). Top: Kinetic traces at the indicated wavelengths (dots) and fit results (solid lines). Middle: Evolution associated spectra (EAS, left), decay associated spectra (DAS, middle) and species associated spectra (SAS, right) along with the scaled differential spectrum for oxidation of [Fe(II)(phtmeimb)$_2$] to [Fe(III)(phtmeimb)$_2$]$^+$ (dashed line). Target analysis (right) assumes 45/45/10% branching of the initially populated unresolved precursor (*MLCT) into 3MLCT, 3MC, and the persistent (>0.8 ns) product species (P). Bottom: Normalized kinetics for the three models.

Electrochemically in situ reduced sample

Complementary transient absorption measurements were performed on electrochemically *in situ* reduced samples in MeCN solution. Excitation power was restricted to < 1 mW to minimize irreversible photobleaching of the sample that became very prominent with more intense illumination. The transient absorption spectrum is composed of a ground state bleach signal centered at approximately 360 nm, and broad excited state absorption above 420 nm. Both features decay concomitantly to a large extent within the first ten ps while a minor part of the ground state bleach and some unspecific absorption in the visible remain at the end of the 8 ns time window of the TA measurements. A biexponential fit model (see Figure S10b) for fits of time traces at selected wavelengths) returned decay associated spectra shown in the inset in Figure S10a. The 8 ps component resembles the combined ps features observed for the chemically reduced sample in THF solution. The long-lived component might be associated to photodegradation of the complex, similar to the essentially non-decaying component in chemically reduced samples in THF. While the poor S/N ratio of the TA data obtained with the electrochemically reduced samples precludes a more detailed analysis, it is evident that the rapid excited state decay observed with the chemically reduced samples cannot be attributed to any quenching of a longer-lived excited state by excess reductant or products formed of the latter. Furthermore, the similar results obtained in THF and MeCN solution exclude quenching of the in theory strongly reducing excited state by the latter solvent. The similar results obtained under both conditions indicate that the rapid excited state decay is intrinsic to the complex.

Similarly, photodegradation of [Fe(II)(phtmeimb)$_2$] was not a peculiarity of the chemically reduced samples and therefore not reliant on reactions involving excess reductant or products of the latter.

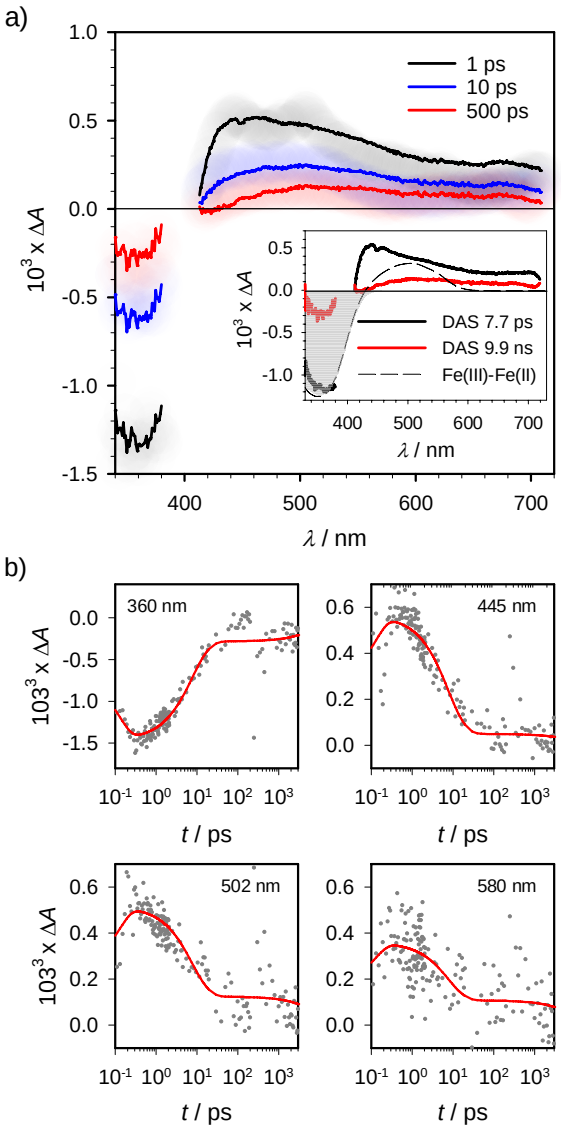

Figure S10: a) fs-TA spectra at selected delay times after excitation of [Fe(II)(phtmeimb)$_2$] at 400 nm shown together with the fit results (solid lines) obtained by global analysis. The inset shows the decay associated spectra together with the scaled differential spectrum for oxidation of [Fe(II)(phtmeimb)$_2$] to [Fe(III)(phtmeimb)$_2$]$^+$ and the pure ground state bleach (shaded area). b) Kinetic traces at the indicated wavelengths together with fit results from global analysis (solid lines).

Computational Methods

Structure optimization and excited state calculations

Density functional theory (DFT) calculations utilizing the B3LYP functional[5] with Grimme's D2 dispersion correction[6] were employed to optimize structure of the singlet ground state (^{1}A), as well as the triplet and quintet metal-centered states (^{3,5}MC) and triplet metal-to-ligand charge transfer (^{3}MLCT) states of $[Fe(phtmeimb)_2]^0$ complex, and doublet ground state of $[Fe(phtmeimb)_2]^+$ complex. The 6-311G* basis set was used for all atoms (H, B, C, N)[7, 8] except for Fe, where the SDD basis sets and its accompanying pseudopotential[9] was employed in all calculations. Solvent effects (acetonitrile) were included in all the calculations via the polarizable continuum model (PCM).[10] Vibrational frequency analysis was performed to ensure that the optimized structures correspond to minima on their respective potential energy surfaces. This particular model chemistry was chosen as it was successfully employed to study electronic structure of similar Fe(II) complexes in the past[11]. Time-dependent DFT (TD-DFT)[12] calculations at the same level of theory as the structure optimizations were employed to simulate the UV-Visible absorption spectra in acetonitrile. The stick spectra were broadened using Lorentzian functions with a half-width-at-half-maximum (HWHM) of 0.12 eV. Fragment molecular orbital analysis (FMOA) based on the Mulliken population analysis was carried out with the AOMix software[13, 14] in order to obtain the percent contributions of each fragment. A three-fragment scheme is employed: Fragment 1 (Fe), Fragment 2 (aryl ring), Fragment 3 (carbene). All calculations were carried out using the Gaussian 16, Revision A.03 software package.[15]

Potential energy surface (PES) diagram

A potential energy surface (PES) diagram based on harmonic curve fits in the diabatic perspective using GS, ^{3}MLCT and ^{3}MC energies together with corresponding cross-energies identified from inspection of the lists of higher singlet-to-triplet TD-DFT excited states.

Harmonic approximation[16] was employed to obtain the potential energy surfaces of ^{3}MLCT and ^{3}MC states that were then used to evaluate Marcus theory parameters. To apply this approximation, consider an illustrative example of two quadratic energy surfaces, as shown in Figure S10. The surfaces are defined by Eqs. (1) and (2) and depend on a single nuclear coordinate *R* (in this case, the average M-L bond length):

$$E_1(R) = \frac{1}{2} k_1 (R - R_1)^2 + c_1 \quad (1)$$

$$E_2(R) = \frac{1}{2}k_2(R - R_2)^2 + c_2 \quad (2)$$

In the above, $E_i(R)$ corresponds to the energy of the potential energy surface i (i = 1, 2) at any specific point along the reaction coordinate R. The R_1 and R_2 are the average M-L bond lengths obtained at the DFT-optimized structures of ^{3}MLCT (R_1) and ^{3}MC (R_2). The energies of the ^{3}MC and ^{3}MLCT states at R_1 and R_2 were then obtained via TD-DFT calculations at the DFT-optimized structures utilizing the ^{1}GS as the reference state, giving the values $E_i(R_i)$. Note that the constants are given by the value of the parabolas at their minima, $c_1 = E_1(R_1)$ and $c_2 = E_2(R_2)$ The parameters k_i were then obtained from Eqns. 1 and 2 as:

$$k_1 = 2\frac{E_1(R_2) - E_1(R_1)}{(R_2 - R_1)^2} \quad (3)$$

$$k_2 = 2\frac{E_2(R_1) - E_2(R_2)}{(R_1 - R_2)^2} \quad (4)$$

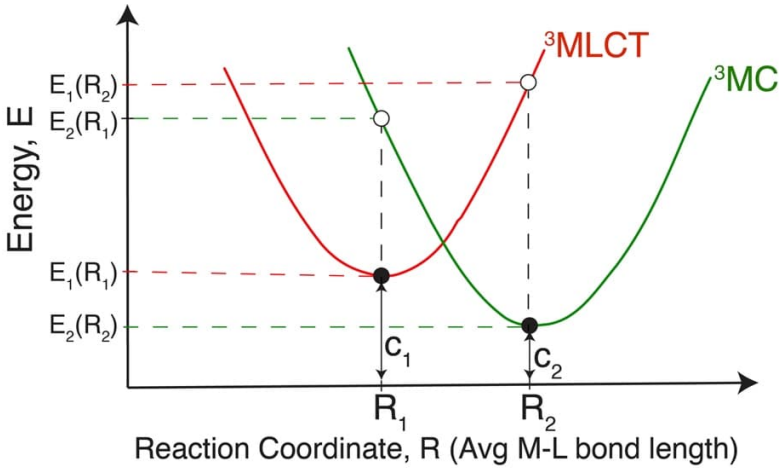

Figure S11. Generic harmonic potential energy curves for ^{3}MLCT (in red) and ^{3}MC (green) as a function of the reaction coordinate R that corresponds to average M-L bond lengths.

Based on these PES surfaces, thermodynamic and kinetic parameters such activation energies (ΔE_{act}), driving force (ΔE), reorganization energy (λ), and electronic coupling matrix (H_{AB}) relevant to the internal conversion of the ^{3}MCT into ^{3}MC were calculated (see Table S3). The activation energies (ΔE_{act}) were

calculated as the difference between the minimum of the ^{3}MLCT and the crossing point of the ^{3}MLCT/^{3}MC. The driving force (ΔE) were obtained from the difference between the minima of the different spin states (^{3}MLCT and ^{3}MC). For the reorganization energy (λ), two different ways can be employed: starting from the reactant, λ(R), or the product λ(P). For λ(R), this was obtained by subtracting the optimized reactant energy from the single point energy calculation performed with the reactant spin state at the product geometry; while λ(P) was obtained by subtracting the optimized product energy from the single point energy calculation performed with the product spin state at the reactant geometry.[17, 18] The two values calculated were then averaged using the arithmetic mean of λ(P) and λ(R).[17, 19] The electronic coupling vector (H_{AB}) was obtained by performing a triplet TD-DFT calculation at the ^{3}MLCT optimized geometry.[20] The NAC keyword and the root (in this case root=1) of the lowest ^{3}MC state was specified in the route section of the input file for TD-DFT calculations.

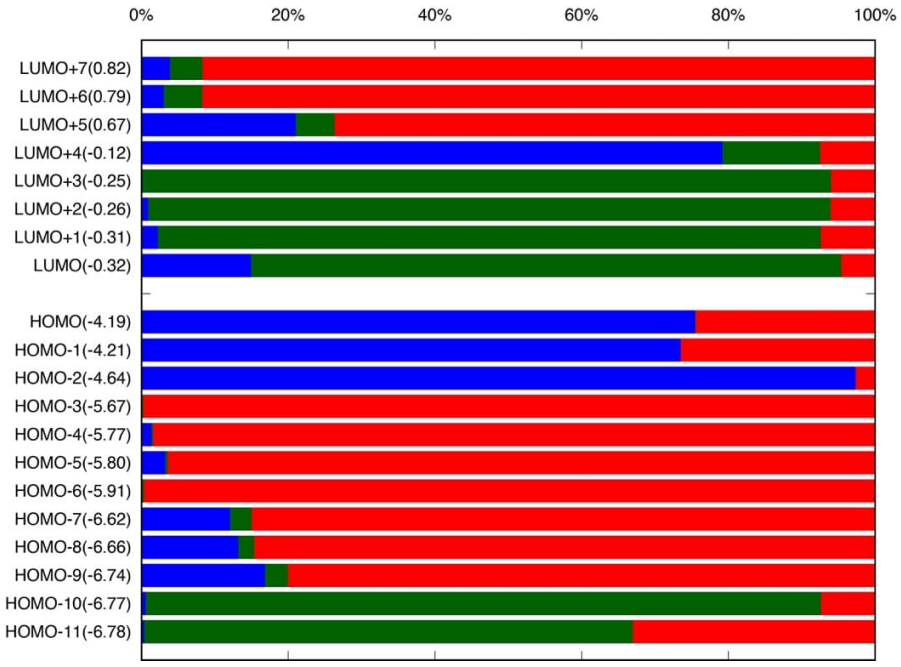

Figure S12: Fragment molecular orbital analysis (HOMO-11 to LUMO+7) of the singlet ground state of [Fe(II)(phtmeimb)$_2$] using B3LYP+D2/6-311G*, SDD(Fe) in acetonitrile. Blue denotes metal based, green aryl based and red carbene based orbitals.

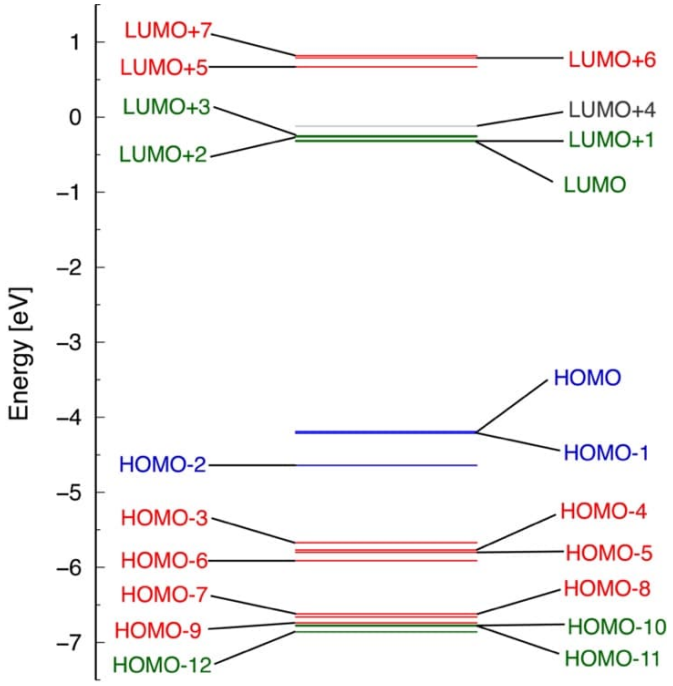

Figure S13: Calculated molecular orbital energy level diagram of the singlet ground state of [Fe(II)(phtmeimb)$_2$] using B3LYP+D2/6-311G*, SDD(Fe) in acetonitrile. Lines in blue are metal based (t_{2g}) in character, green are aryl-based, red are carbene-based orbitals, and grey is a Rydberg-type d-orbital.

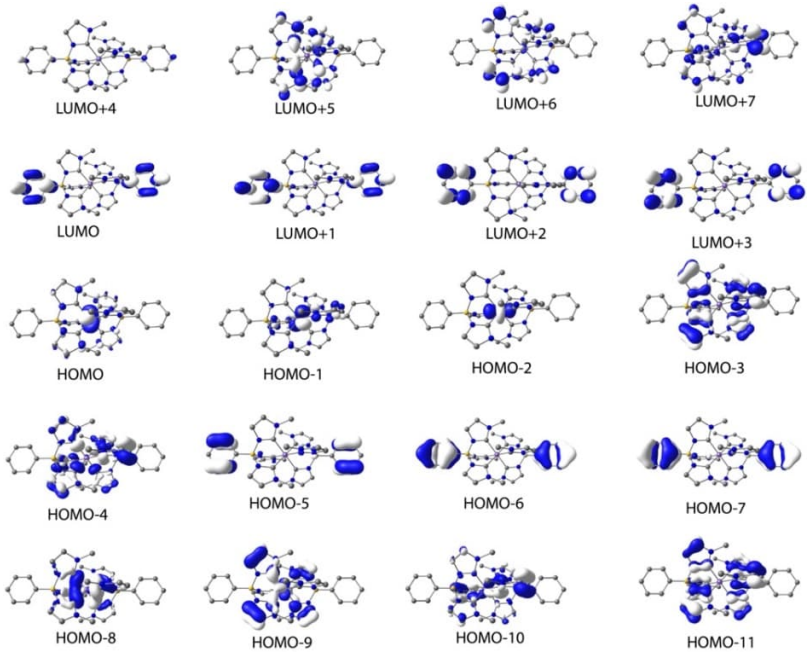

Figure S14: Molecular orbital pictures (HOMO-11 to LUMO+7) of the singlet ground state of [Fe(II)(phtmeimb)$_2$] at B3LYP+D2/6-311G*, SDD(Fe) level of theory in acetonitrile. Contour isovalue of 0.04 Å/e.

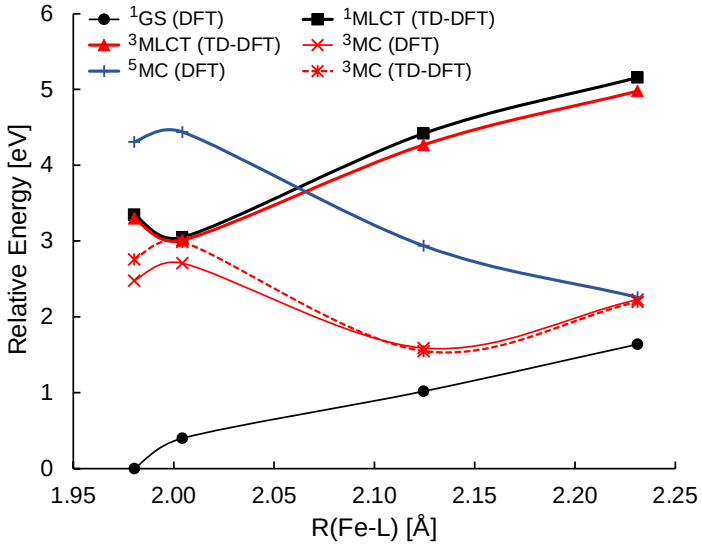

Figure S15. Potential energy curves for the relevant electronic states of [Fe(II)(pthmeimb)$_2$] from energies obtained at the ^{1}GS (R = 1.98 Å), ^{3}MLCT (R = 2.00 Å), ^{3}MC (R = 2.12 Å), and ^{5}MC (R = 2.23 Å) optimized structures from single point energy calculations at the DFT (^{1}GS, ^{3}MC, ^{5}MC) and TD-DFT levels of theory (^{1,3}MLCT, ^{3}MC) utilizing ^{1}GS as the reference state. The reaction coordinate is given as the average of Fe-L bond lengths at each optimized structure.

Table S1: Quantum calculated relaxed states for [Fe(II)(pthmeimb)$_2$] complex at B3LYP+D2/6-311G*, SDD(Fe) level of theory in acetonitrile.

Geometry	E(eV)	Fe spin density	R_{avg} (Fe-C) (Å)
^{1}GS	0.00	-	1.98
^{3}MLCT	2.28	1.083	2.004
^{3}MC	1.89	2.024	2.125
^{5}MC	2.15	3.683	2.231

Table S2: Quantum calculated relative energies (in eV) of the various states for [Fe(pthmeimb)$_2$] complex with B3LYP+D2/6-311G*, SDD(Fe) level of theory in acetonitrile at the fully relaxed ^{1}GS, ^{3}MLCT, ^{3}MC and ^{5}MC geometry.

		Relative Energies (in eV)					
	Fe-C (Å)	^{1}GS (DFT)	^{1}MLCT (TD-DFT)	^{3}MLCT (TD-DFT)	^{3}MC (DFT)	^{3}MC(TD-DFT)	^{5}MC (DFT)
^{1}GS	0.00	0.00	3.35	3.30	2.48	2.76	2.76
^{3}MLCT	0.04	0.40	3.05	3.01	2.71	2.99	2.99
^{3}MC	0.14	1.02	4.42	4.27	1.59	1.55	1.55
^{5}MC	0.25	1.64	5.16	4.98	2.23	2.20	2.20

Electronic Absorption Spectra

The simulated absorption spectra are similar to the experimentally observed spectra for both the Fe(II)- and Fe(III)-complexes. For the Fe(II)-complex, the lowest energy transitions are metal-to-ligand charge transfer (MLCT) in character, with the major peak around 300 nm being composed of a metal (t_{2g}) to carbene π^* transitions. For the Fe(III)-complex, the major transition is a ligand-to-metal charge transfer (LMCT), which occurs around 400 nm and involves a carbene π to metal transition.

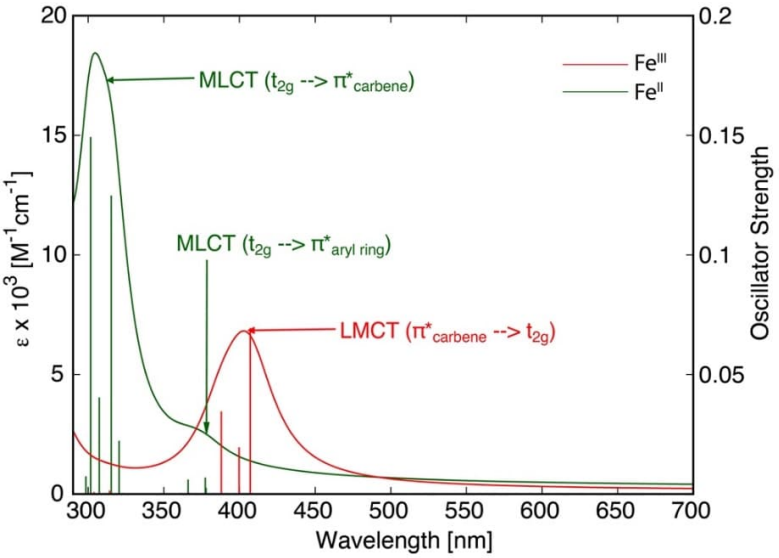

Figure S15: Calculated electronic absorption spectra of Fe(II)- (green) and Fe(III)- (red) complexes of phtmeimb$^-$ at B3LYP+D2/6-311G*(C,H,N,B), SDD(Fe) level of theory in acetonitrile. MLCT denotes metal-to-ligand charge transfer and LMCT denotes ligand-to-metal charge transfer.

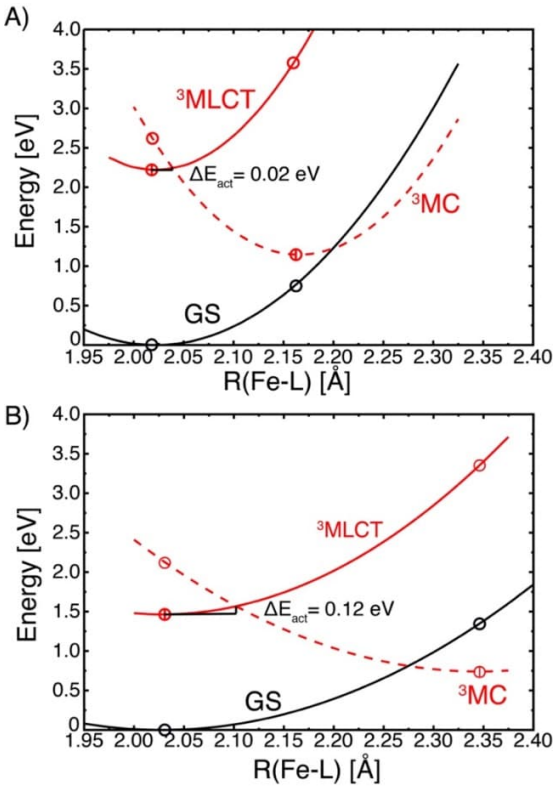

Figure S16: Extrapolated diabatic harmonic singlet and triplet potential energy surfaces for [Fe(II)(phtmeimb)$_2$] (A) and [Fe(II)(btz)$_3$]$^{2+}$ (B) along an effective one-dimensional average Fe-C reaction coordinate calculated at B3LYP*/6-311G(d,p) level of theory in acetonitrile.

Table S3: Calculated thermodynamic parameters for $[Fe(II)(btz)_3]^{2+}$ and $[Fe(II)(phtmeimb)_2]$ complexes at B3LYP+D2/6-311G*(C,H,N,B), SDD(Fe) level of theory in acetonitrile.

	ΔE_{act} (eV)	ΔE (eV)	λ (R) (eV)	λ (P) (eV)	λ (A)(eV)	H_{AB} ($Bohr^{-1}$)
[Fe(phtmeimb)]	0	-1.45	1.26	1.43	1.35	0.0829
$[Fe(btz)]^{2+}$	0.07	-1.09	2.03	1.74	1.89	0.0263

References

1. K. S. Kjaer, N. Kaul, O. Prakash, P. Chabera, N. W. Rosemann, A. Honarfar, O. Gordivska, L. A. Fredin, K. E. Bergquist, L. Häggström, T. Ericsson, L. Lindh, A. Yartsev, S. Styring, P. Huang, J. Uhlig, J. Bendix, D. Strand, V. Sundström, P. Persson, R. Lomoth and K. Wärnmark, *Science*, 2019, 363, 249-253.
2. K. L. Materna, N. Lalaoui, J. A. Laureanti, A. P. Walsh, B. P. Rimgard, R. Lomoth, A. Thapper, S. Ott, W. J. Shaw, H. Tian and L. Hammarstrom, *ACS Appl Mater Interfaces*, 2020, 12, 4501-4509.
3. L. van Turnhout, Y. Hattori, J. Meng, K. Zheng and J. Sa, *Nano Lett*, 2020, 20, 8220-8228.
4. J. J. Snellenburg, S. P. Laptenok, R. Seger, K. M. Mullen and I. H. M. v. Stokkum, *J Stat Softw*, 2012, 49.
5. A. D. Becke, *Phys Rev A Gen Phys*, 1988, 38, 3098-3100.
6. S. Grimme, *J Comput Chem*, 2006, 27, 1787-1799.
7. R. Krishnan, J. S. Binkley, R. Seeger and J. A. Pople, *J Chem Phys*, 1980, 72, 650-654.
8. A. D. McLean and G. S. Chandler, *J Chem Phys*, 1980, 72, 5639-5648.
9. M. Dolg, U. Wedig, H. Stoll and H. Preuss, *J Chem Phys*, 1987, 86, 866-872.
10. G. Scalmani and M. J. Frisch, *J Chem Phys,* 2010, 132, 114110.
11. D. C. Ashley and E. Jakubikova, *Inorg Chem*, 2018, 57, 5585-5596.
12. M. E. Casida, C. Jamorski, K. C. Casida and D. R. Salahub, *J Chem Phys*, 1998, 108, 4439-4449.
13. Gorelsky, S. I. AOMix: Program for Molecular Orbital Analysis; version 6.94., (http://www.sg-chem.net/).
14. Gorelsky, S. I., AOMix: Program for molecular orbital analysis. 1997.
15. M. J. Frisch, G. W. Trucks, H. B. Schlegel, G. E. Scuseria, M. A. Robb, J. R. Cheeseman, G. Scalmani, V. Barone, G. A. Petersson, H. Nakatsuji, X. Li, M. Caricato, A. V. Marenich, J. Bloino, B. G. Janesko, R. Gomperts, B. Mennucci, H. P. Hratchian, J. V. Ortiz, A. F. Izmaylov, J. L. Sonnenberg, Williams, F. Ding, F. Lipparini, F. Egidi, J. Goings, B. Peng, A. Petrone, T. Henderson, D. Ranasinghe, V. G. Zakrzewski, J. Gao, N. Rega, G. Zheng, W. Liang, M. Hada, M. Ehara, K. Toyota, R. Fukuda, J. Hasegawa, M. Ishida, T. Nakajima, Y. Honda, O. Kitao, H. Nakai, T. Vreven, K. Throssell, J. A. Montgomery Jr., J. E. Peralta, F. Ogliaro, M. J. Bearpark, J. J. Heyd, E. N. Brothers, K. N. Kudin, V. N. Staroverov, T. A. Keith, R. Kobayashi, J. Normand, K. Raghavachari, A. P. Rendell, J. C. Burant, S. S. Iyengar, J. Tomasi, M. Cossi, J. M. Millam, M. Klene, C. Adamo, R. Cammi, J. W. Ochterski, R. L. Martin, K. Morokuma, O. Farkas, J. B. Foresman and D. J. Fox, Gaussian, Inc., Wallingford CT, 2016.
16. T. Chachiyo and J. H. Rodriguez, *J Chem Phys*, 2005, 123, 94711.

17. S. M. Fatur, S. G. Shepard, R. F. Higgins, M. P. Shores and N. H. Damrauer, *J Am Chem Soc*, 2017, 139, 4493-4505.
18. G. Basu, A. Kitao, A. Kuki and N. Go, *J Phys Chem B*, 1998, 102, 2076-2084.
19. O. López-Estrada, H. G. Laguna, C. Barrueta-Flores and C. Amador-Bedolla, *ACS Omega*, 2018, 3, 2130-2140.
20. I. Tavernelli, B. F. Curchod, A. Laktionov and U. Rothlisberger, *J Chem Phys*, 2010, 133, 194104.